Engineering Structures 295 (2023) 116839

Contents lists available at ScienceDirect

Engineering Structures

journal homepage: www.elsevier.com/locate/engstruct

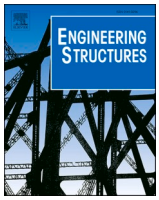

Dynamic response of a steel catenary riser at touch-down zone

Zhenguo Gao [a], Weichen Wang [b], Zefeng Zhou [c,*], Yue Yan [d], Dhruba L. Pradhan [e]

[a] School of Naval Architecture & Ocean Engineering, Jiangsu University of Science and Technology, Zhenjiang 212100, Jiangsu Province, China
[b] Key Laboratory of Marine Environment and Ecology, Ministry of Education, Ocean University of China, 238 Songling Road, Qingdao 266100, China
[c] Advanced Modelling, Offshore Energy, Norwegian Geotechnical Institute (NGI), Sognsvn. 72, 0855 Oslo, Norway
[d] State Key Laboratory of Hydraulic Engineering Simulation and Safety, Tianjin University, Tianjin 300072, China
[e] DNV Energy Systems Z1, Veritasveien 1, 1363 Høvik, Norway

ARTICLE INFO

Keywords:
Steel catenary riser (SCR)
Pipe-soil interaction
Seabed softening
Changing soil strength
Seabed trench
Fatigue damage

ABSTRACT

This paper introduces a numerical model for analysing the dynamic response and fatigue damage of a global steel catenary riser (SCR) at the touch-down zone (TDZ). The model incorporates an innovative pipe-soil interaction model based on a new effective-stress framework to evaluate the changing soil strength induced by the cyclic motion of the SCR, thereby allowing for a more accurate assessment of the effects of soil remoulding and trenching on the dynamic responses of the SCR. The global SCR model is implemented in a commercial finite element software – ABAQUS, with the pipe-soil interaction model integrated through a user-defined element subroutine. A comprehensive series of time-domain simulations is conducted to investigate the evolution of seabed and the subsequent development of trenching along the seabed pipeline. These simulations provide valuable insights into the structural performance of the SCR at the TDZ. Additionally, this research explores the effects of water entrainment, changing seabed strength & stiffness, and the heaving motion of the floater on the fatigue damage of the global SCR. Understanding these factors is essential for obtaining an extensive understanding of the SCR's behaviour in the TDZ. The findings provide significant insights that can be leveraged to optimise existing design practices and enhance the efficiency and safety of offshore infrastructure.

1. Introduction

A steel catenary riser (SCR) is one of the widely used solutions for transporting hydrocarbon products from the seabed wellhead to the floating facility in deep-water oil and gas field development. One of the main concerns in the SCR design is accurately predicting its fatigue damage induced by cyclic motions of the SCR, especially at the touch-down zone (TDZ). The long-term interaction between the seabed and the SCR at the TDZ has a substantial impact on the dynamic responses and fatigue performance of the SCR, which highlights the significant influence of the seabed conditions, i.e., the soil strength and stiffness [1,2], on the SCR at the TDZ. Therefore, a robust design approach to predict the fatigue of SCR is essential. An efficient global riser model capable of simulating the SCR's dynamic response, along with an accurate pipe-soil model that reflects the nonlinear characteristics of the pipe-soil interaction, are key elements for achieving precise simulations.

Several pipe-soil models have been developed to describe the SCR and seabed interaction response. Most of these models adopt the total stress analysis method [3–5], which calculates the loading paths (i.e., initial penetration, uplift, break contact, and re-penetration) using different hysteretic models – either with closed or open hysteresis loops (as shown in Fig. 1), during cyclic SCR motions [6–9]. In the 'closed-loop' model, the re-penetration will intersect the point where the pipe turns for extraction, resulting in a closed hysteretic loop. On the other hand, the 'open-loop' model accounts for the additional penetration that occurs during the re-penetration process. The models of capturing the progressive penetration behaviours of the SCR typically adopt a formulation for the load–displacement response, without directly considering the degradation of natural soil strength and stiffness induced by cyclic loading. As a result, they cannot explicitly link seabed properties to the change in soil effective stress associated with excess pore pressure generation induced by undrained cyclic shearing. A new pipe-soil interaction model is recently reported by Zhou et al. [29]. The model is based on the effective-stress framework [10–12] using the critical state soil mechanics, simplifying the calculation process by linking the soil strength to changes in effective stress during cyclic loading. The complex load–displacement of an SCR segment can be

* Corresponding author.
E-mail addresses: zhenguo.gao@just.edu.cn (Z. Gao), wwc_0813@stu.ouc.edu.cn (W. Wang), Zefeng.zhou@ngi.no (Z. Zhou), yue.yan@tju.edu.cn (Y. Yan), dhruba.lal.pradhan@dnv.com (D.L. Pradhan).

https://doi.org/10.1016/j.engstruct.2023.116839
Received 13 June 2023; Received in revised form 14 August 2023; Accepted 29 August 2023
Available online 8 September 2023

Notations

C_a	added mass coefficient
C_d	drag coefficient
D	diameter of penetrating SCR
D_b	accumulated fatigue damage
F_h	hydrodynamic forces
H	heave motion amplitude
k	seabed strength gradient
K	tangent stiffness
K_{max}	maximum tangent stiffness adopted since the last reversal in penetration or extraction
N	allowable number of cycles to failure
N_c	bearing capacity factor
$N_{T\text{-}bar}$	bearing capacity factor of T-bar
p	parameter for pore pressure generation rate
q	SCR penetration resistance
q_s	seabed resistance
q_b	soil buoyancy
s_u	undrained shear strength
$s_u(\widehat{z})$	undrained shear strength profile
$s_{u,i}$	in-situ undrained shear strength
$s_{u,av}$	average undrained shear strength
$s_{u,cyc}$	cyclic undrained shear strength
$s_{u,mob}$	mobilised soil strength
S_t	soil sensitivity
$(s_u/\sigma'_{v0})_{NC}$	normally consolidated undrained strength ratio
u_e	excess pore pressure profile
$u_{e,r}$	remaining potential excess pore pressure profile
$u_{e,max}$	maximum excess pore pressure profile
v_s	strength influence function
v	specific volume
$v_{initial}$	initial specific volume
z	soil depth
$\widehat{z}$	normalised soil depth, z/D
z_e	depth of reference point of penetrating object below soil surface
$\widehat{z}_e$	normalised depth, z_e/D
α	strength influence zone extent
β	strain influence zone extent
χ	characteristic pressure
η	load sharing factor
λ	gradient of the normal consolidation line (NCL)
κ	gradient of the unload-reload line (URL)
Φ	lumped strength parameter
Φ_{steady}	steady value of lumped strength parameter
k_Φ	strength parameter multiplier
ρ	water density
σ_a	axial stress
σ_b	bending stress
σ_c	stress range
σ'_v	vertical effective stress
$\sigma'_{v,eqm}$	equilibrium vertical effective stress
$\sigma'_{v,NCL}$	vertical effective stress at NCL
$\sigma'_{v,RSL}$	vertical effective stress at RSL
σ'_{v0}	in situ geostatic effective stress
ε	cumulative (absolute) shear strain
ε_{99}	cumulative (absolute) shear strain required for a degree of remoulding equal to 99%
$\varepsilon_{95,\Phi}$	peak strength ductility parameter
$\mu(\widehat{z})$	strain influence distribution function
Ψ	vertical distance between the object penetration depth and a given soil horizon normalised by the object diameter
Λ	plastic volumetric strain ratio
Γ_{NCL}	specific volume, v, $\sigma'_v = 1$ kPa on the NCL
ς	nonlinear tangent stiffness parameter
γ'	soil effective unit weight

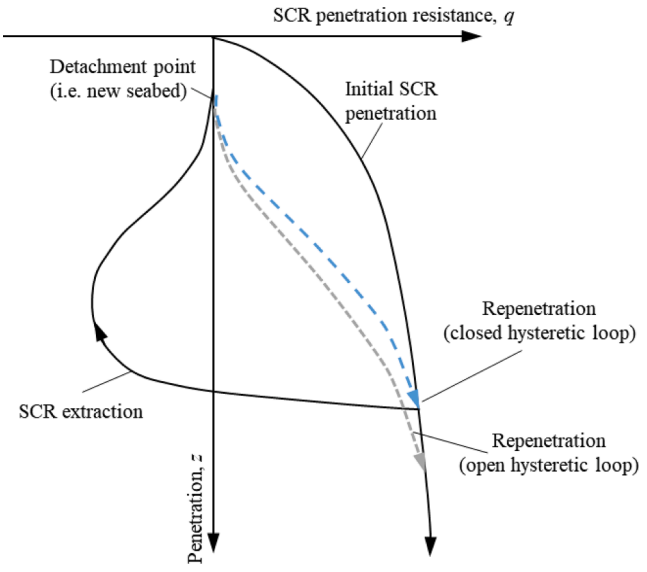

Fig. 1. Typical pipe-soil models [6,8].

captured by a simple equation. This model can be potentially adopted to pursue a more comprehensive understanding of the pipe-soil interaction and its impact on the SCR's overall performance.

For global simulation of the global riser system, a few studies have been conducted by utilising either the quasi-static or dynamic methods as summarised in Table 1. The AB model was initially utilised for the global riser analysis, while the RQ model has been widely applied later. The RQ model has been incorporated in commercial software such as

Table 1
A summary of global SCR studies.

Global analysis	Pipe-soil model	Stress domain	Changing soil strength	Analysis method
Aubeny and Biscontin [6]	AB[a] model	Total stress	No	Quasi-Static
Shiri and Randolph [13]	RQ[b] model			
Elosta et al. [14]				Dynamic
Bai et al. [15]				
Liu et al. [16]				
Dong and Shiri [17]				
Zhao et al. [18]	Elastoplastic model	Effective stress	Yes	Quasi-Static
Janbazi and Shiri [19]	Proposed by Hodder et al. [11]			Dynamic
This study	Proposed by Zhou et al. [10]			Dynamic in time domain

[a] Aubeny and Biscontin [6].
[b] Randolph and Quiggin [8].

Orcaflex and has also been redeveloped in other software packages. Bai et al. [15] implemented the RQ model into Cable3D RSI to conduct the dynamic analysis of SCR at the TDZ in the time domain. Dong and Shiri [17] identified several limitations in the RQ model, specifically with regard to the global response of the SCR. These limitations include an overestimation of the penetration embedment and cyclic contact stress, as well as an inability to explicitly model trench development (reported by Yuan et al. [34] and Rui et al. [39]). Zhao et al. [18] performed a simple steady-state analysis of a SCR system, by combing an elasto-plastic model and the effective stress framework [10] to investigate the SCR-seabed interaction under a quasi-static condition. Janbazi and Shiri [19] conducted a dynamic analysis for the global riser system using an effective stress framework [11] to investigate the effect of soil consolidation on the fatigue performance of SCR. In general, the findings from various studies on the global riser system analysis indicate that the cyclic motions of the floater result in stress concentration of the SCR at the TDZ. However, consideration of both the dynamic responses of the global SCR and the changing seabed properties induced by corresponding dynamic loading (as shown in Fig. 2) remains limited in existing analyses. Yet the changing soil strength is not taken into account in the global riser analysis in many of the studies reviewed above.

In the present study, the dynamic response and fatigue performance of an SCR at the TDZ is investigated by proposing a global SCR model with the novel pipe-soil model incorporated [10]. The novel pipe-soil model, which is based on the effective stress concept, is implemented into the global SCR model in ABAQUS. The proposed global SCR model is capable of describing the complex nonlinear features of the pipe-soil interaction and simulating the dynamic response of the global riser. After verification, the influence of the floater heave motion, seabed properties, and water entrainment effect on the response of the global riser is examined by performing dynamic simulations in the time domain. The parameters, including the riser embedment profile, effective stress degradation, distribution of stress and bending moment, and cumulative fatigue damage are analysed. The valuable insights for the design and optimization of subsea riser systems are provided based on the findings of this study.

2. Pipe-soil interaction model

This study utilises a newly proposed effective-stress framework developed by Zhou et al. [10] to accurately depict the dynamic pipe-soil interaction. Based on the principles of critical-state soil mechanics [20], this framework appropriately accounts for the variations in soil effective stress caused by the cyclic-loading-induced pore water pressure. As a result, it can capture the natural response of the seabed along the SCR during complex cyclic loading, deviating from conventional methods that rely on a reduction factor for the entire seabed at the touch-down zone (TDZ). To model the pipe-soil system, the seabed is discretised into a one-dimensional column, as illustrated in Fig. 2. Instead of employing oversimplified soil springs [13], specific soil properties are assigned to individual soil elements. This approach enhances the representation of the dynamic behavior of the pipe-soil system, allowing for a more comprehensive analysis. The soil experiences periodic vertical loading & unloading and the analytical components of this process are briefly outlined in this section, as shown in Fig. 3. More detailed descriptions can be found in Zhou et al. [10].

2.1. Changes in the effective stress of seabed due to cyclic loading

The excess pore pressure generation during undrained cyclic loading, $u_e(\hat{z})$ (where $\hat{z} = z/D$ is the normalised penetration depth; D is the SCR diameter), is linked to the cumulative plastic strain $\varepsilon(\hat{z})$ at each soil domain, as shown in Fig. 3(a). The rate of excess pore pressure generation can be calculated as

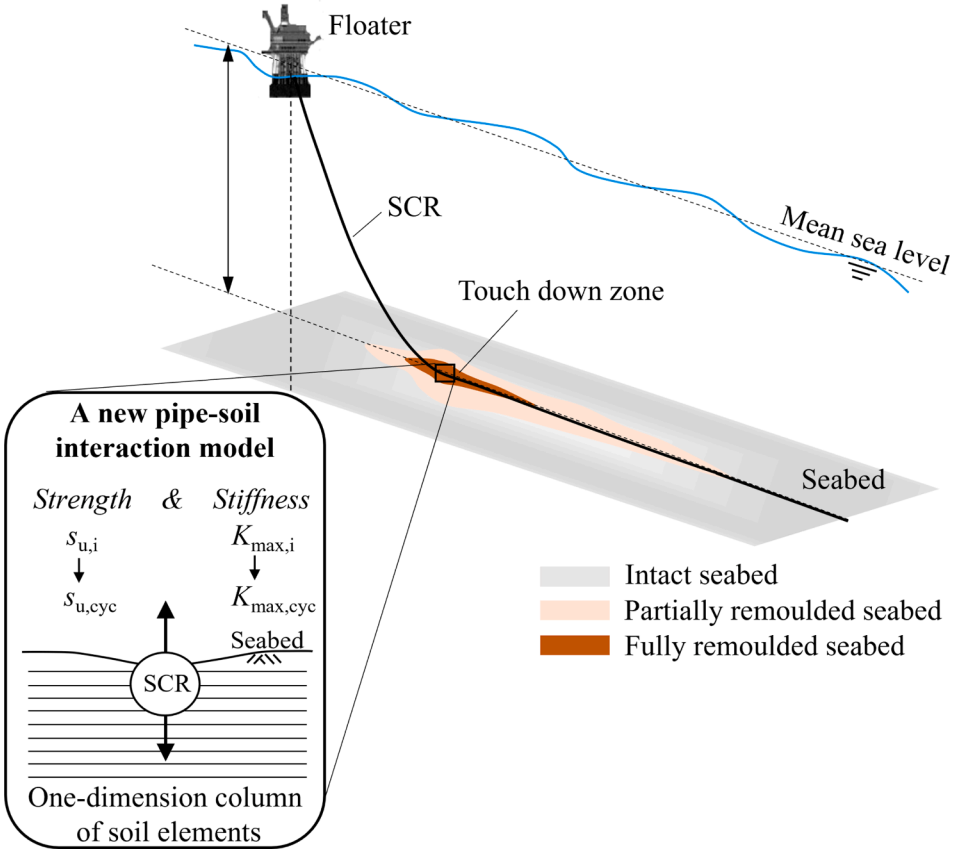

Fig. 2. The effective stress framework for SCR-seabed interaction.

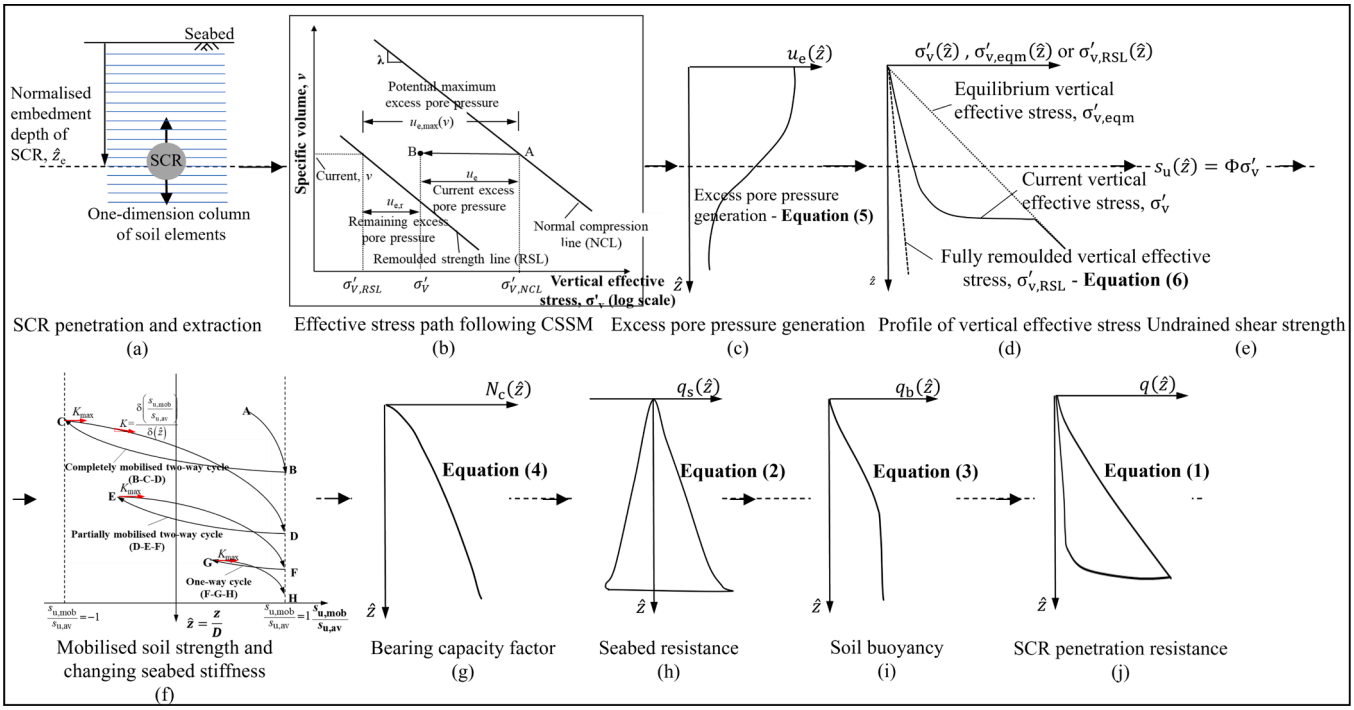

Fig. 3. The analytical components of the effective-stress model [10].

$$\frac{\delta u_e(\hat{z})}{\delta\varepsilon(\hat{z})} = \frac{\chi}{\varepsilon_{99}}\left[\frac{u_{e,r}(\hat{z})}{u_{e,max}(\hat{z})}\right]^p = \frac{\chi}{\varepsilon_{99}}\left[\frac{\sigma'_v(\hat{z}) - \sigma'_{v,RSL}(\hat{z})}{\sigma'_{v,NCL}(\hat{z}) - \sigma'_{v,RSL}(\hat{z})}\right]^p \quad (1)$$

where the incremental cumulative shear strain is related to the progressive embedment of the object $\delta\hat{z}_m$, and is expressed by the weighted influence function, $\delta\varepsilon(\hat{z}) = 4\mu(\hat{z})\delta\hat{z}_m$ (details seen in Zhou et al. [10]); $\chi = \frac{(1-0.01^{1-p})}{1-p}u_{e,max}(\hat{z})$ is a characteristic pressure; ε_{99} is the characteristic shear strain implying a 99% degree of strength degradation from intact to fully cyclic remoulded soil state; p is a constant power controlling the shape of the pore pressure generation; $u_{e,r}$ is the remaining excess pore pressure equal to the distance between the current vertical effective stress σ'_v and the effective stress on the RSL $\sigma'_{v,RSL}$; $u_{e,max}$ represents the maximum potential excess pore pressure, $u_{e,max} = \sigma'_{v,NCL} - \sigma'_{v,RSL}$ (where $\sigma'_{v,NCL}$ is the effective stress on the NCL) as shown in Fig. 3(b); The vertical effective stress on the RSL $\sigma'_{v,RSL}$ is proposed by Zhou et al. [10] and Hodder et al. [11] as

$$\sigma'_{v,RSL}(\hat{z}) = \left(\frac{s_u}{\sigma'_{v0}}\right)_{NC}\frac{\sigma'_{v0}(\hat{z})}{\Phi S_t}exp\left\{\frac{\Lambda\left[\Gamma_{NCL} - v_{initial}(\hat{z}) - \lambda ln\left(\sigma'_{v0}(\hat{z})\right)\right]}{\lambda - \kappa}\right\} \quad (2)$$

where $(s_u/\sigma'_{vo})_{NC}$ is the normally consolidated undrained strength ratio; Λ is the plastic volumetric strain ratio; Γ_{NCL} is the specific volume at $\sigma'_v = 1$ kPa on the NCL; $v_{initial}$ is the initial specific volume; λ and κ are the gradients of NCL and URL, respectively; S_t is the soil sensitivity; Φ is a lumped strength parameter linked to cumulative shear strain [10]. The distributions of vertical spatial profile of excess pore pressure are shown in Fig. 3(c).

2.2. Changing seabed stiffness and mobilisation of soil strength

The undrained shear strength s_u, at each soil depth, is acquired from the current vertical effective stress through a lumped strength parameter Φ

$$s_u(\hat{z}) = \Phi\sigma'_v(\hat{z}) \quad (3)$$

where $\sigma'_v(\hat{z}) = \sigma'_{v,eqm}(\hat{z}) - u_e(\hat{z})$, as shown in Fig. 3(d). An average undrained shear strength in the vicinity of the current depth of the SCR $s_{u,av}$, can be calculated by the integration of the current soil strength

$$s_{u,av} = \int_{\hat{z}_e-\alpha}^{\hat{z}_e+\alpha} s_u(\hat{z})v_s(\hat{z})dz \quad (4)$$

where $v_s(\hat{z})$ is a strength influence function, α is the influence extent above and below the centreline of the SCR.

A nonlinear strength-displacement model is utilised to capture the soil strength mobilization as the motion reversal occurring by way of an exponentially decaying tangent stiffness K

$$\delta\left(\frac{s_{u,mob}}{s_{u,av}}\right) = \delta(\hat{z})K \quad (5)$$

The determination of tangent stiffness K, is related to the proportion of the change in mobilised strength

$$K = \left\{1 - \left[\frac{\Delta\left(\frac{s_{u,mob}}{s_{u,av}}\right)}{\Delta\left(\frac{s_{u,max}}{s_{u,av}}\right)}\right]^{\zeta}\right\}K_{max} \quad (6)$$

where $\left(\frac{|\Delta s_{u,mob}|}{s_{u,av}}\right)$ is the current normalised strength change varying from −1 to 1, $\left(\frac{|\Delta s_{u,max}|}{s_{u,av}}\right)$ is the potential normalised strength change lying in the range 0–2, as shown in Fig. 3(f); ς is the power factor to control the rate of change in tangent stiffness; K_{max} is the maximum tangent stiffness as the last one-way or two-way cyclic reversal motion occurs.

2.3. Changes in penetration resistance of SCR element at the TDZ

In general, the penetration resistance of the SCR element q, is composed of seabed resistance q_s (see Fig. 3(h)) and soil buoyancy q_b (see Fig. 3(i)).

$$q(\hat{z}) = q_s(\hat{z}) + q_b(\hat{z}) \quad (7)$$

in which

$$q_s(\widehat{z}) = N_c s_{u,av} \tag{8}$$

and

$$q_b(\widehat{z}) = f_b A_s \gamma' \frac{1}{D} \tag{9}$$

$s_{u,av}$ in equation (8) is the average undrained shear strength derived from the framework, and N_c (see Fig. 3(g)) is the bearing capacity factor varing with the soil depth

$$N_c = a(\widehat{z})^b \tag{10}$$

where $a = 7.1$ and $b = 0.33$ for $\widehat{z} \leq 0.75$ [21] and $a = 6$ and $b = 0.15$ for $\widehat{z} > 0.75$ [22].

The soil buoyancy q_b, in Eq. (9) is based on Archimedes' principle, which is linked to the effective unit weight of soil γ', the normalised cross-sectional area of the submerged segment of the SCR A_s, and a factor f_b.

2.4. Reduction in soil strength due to water entrainment

In this study, the influence of water entrainment on the strength of the seabed near the water-mudline interface is captured, where the ongoing motion of the SCR is approaching or crossing.

To capture this phenomenon within the effective-stress framework, adjustments are made by increasing the soil sensitivity, S_t, and shifting the RSL to the left (i.e. the low effective stress level). This approach results in a reduction in effective stress and soil strength after cyclic remoulding, allowing for the modeling of lower soil strength due to water entrainment. Consequently, the formation of a seabed trench along the SCR can be accounted for. This investigation provides insights into the dynamic response and fatigue damage of the global riser system in the vicinity of the water-mudline interface. By considering the effects of water entrainment, changes in soil strength, and the resulting trench formation, a more comprehensive understanding of the system's behavior under dynamic conditions is achieved. It's also worth noting that seabed erosion can be influenced by a range of factors, encompassing subsea currents induced vortices, dynamic motion of the pipe at TDZ, properties of seabed, etc. Thus, in-depth investigation into the effects of water entrainment requires further refinement in future studies.

3. Global riser model

In this section, the global riser model is presented with the application of the novel pipe-soil model for the on-bottom portion. The global model has been implemented using the commercial software ABAQUS (2010) [23], which is widely used for the analysis of SCRs [24–26].

3.1. Details of the model and analysis procedures

A global SCR model is developed based on the structural properties listed in Table 2. As schematically illustrated in Fig. 2, the SCR has a typical configuration connected to a Spar platform. The total length of the SCR is 2000 m, and the outer diameter of the riser is 0.457 m. The operating water depth is 935 m. The SCR is modelled with a 2-node Euler-Bernoulli beam element. The mesh size of the SCR is 1.0 m except for the riser segment of 600–1000 m to the anchor point, which is supposed to be located at the touch-down region and a mesh size of 0.5 m is selected.

The hydrodynamic forces (including the drag force and inertia force) acting on the SCR are calculated with the Morison equation [27], which can be expressed as

Table 2
Details of the SCR parameters.

Parameters	Values
SCR total length	2000 m
Outer diameter	0.457 m
Inner diameter	0.415 m
Wall thickness	0.021 m
Elastic modulus	207 GPa
Poisson Ratio	0.3
Riser density in air	7850 kg/m^3
Submerged Weight	1000 N/m
Height of hang-off point	920 m
Hang-off angle	15.7 deg.
Water Depth	935 m

$$F_h = \frac{1}{2}\rho D C_d(-\dot{x})|\dot{x}| + \frac{\pi D^2}{4}\rho C_a(-\ddot{x}) \tag{11}$$

where x, $\dot{x}$, $\ddot{x}$ and are the displacement, velocity and acceleration of the riser, respectively; C_d and C_a are the drag and the added mass coefficients, respectively; ρ is the water density. The first term on the right-hand side of Eq. (11) refers to the hydrodynamic damping from the viscous drag force of the water, and the second term is the inertia force, which can change the natural period of the SCR due to the added mass effect.

The Morison equation is inherently built in the AQUA module of ABAQUS. In the present simulations, the drag coefficient is selected to be 0.65 and the added mass coefficient is 1.0 [28]. The buoyance of the riser is considered with the AQUA module as well.

The integration of the pipe-soil interaction model into the global riser analysis is achieved through the implementation of an effective-stress framework model within a user-defined element subroutine. This subroutine, written in Fortran, is compiled as part of the Abaqus User Element Library (UEL). The seabed is modelled as a one-dimensional column of soil elements, with a size of 0.01 m in the vertical direction and 1 m in the horizontal direction, as recommended in previous studies [29] for simulation accuracy. During the pipe-soil interaction, the framework model is utilised to establish the relationship between the seabed reaction force and SCR penetration depth. The cyclic displacement of SCR can also be taken into consideration to evaluate the changing seabed strength and stiffness, which have implications for the distribution of loads along the SCR and the embedded SCR configuration after cyclic loading.

The dynamic analysis methods for risers can be classified into two primary categories: frequency-domain and time-domain methods. Frequency-domain methods offer higher efficiency compared to time-domain methods. However, their applicability is limited to systems exhibiting predominantly linear behaviour. In contrast, time-domain methods enable a comprehensive consideration of nonlinearities, such as nonlinear pipe-soil interactions and hydrodynamics, despite their computationally intensive nature. In the present simulations, dynamic analysis in the time domain is conducted to account for all nonlinear effects. The procedure for analysing the dynamic response of a global SCR in ABAQUS is depicted in Fig. 4. The analysis type, either static or dynamic, is identified at the initiation of the ABAQUS/Standard analysis, and the time increment scheme is determined based on the input file. For each time step, the floater displacement is calculated first, which determines the forced displacement at the top of the SCR. Subsequently, iterations commence attaining displacement and force equilibrium at each node of the SCR. During each iteration, the formation of the global stiffness matrix is required, and the displacements of nodes in contact with the seabed are passed to the UEL subroutine. The seabed stiffness and reaction forces are then calculated utilising a pipe-soil interaction model, which considers the SCR displacements. By including the effects of the seabed stiffness and resistance, the global equilibrium of each node of the SCR is evaluated. If the equilibrium

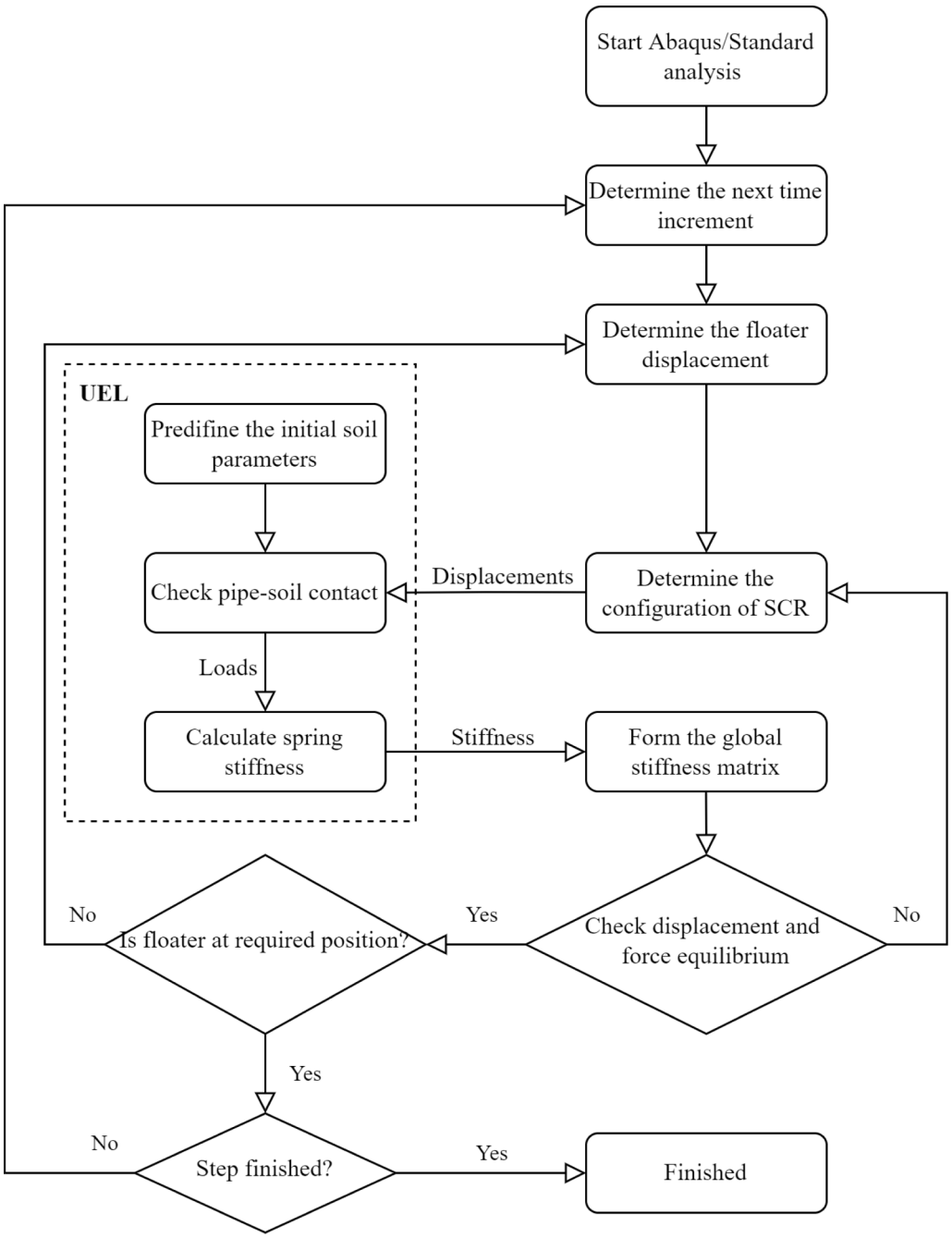

Fig. 4. The flowchart for analysis procedures of the proposed global riser model.

convergence criterion is fulfilled for all nodes, the current time increment concludes, and the next time step commences. The process repeats until the analysis is complete.

For analysis of such a long flexible SCR in ABAQUS, a convergence problem may be encountered due to the high nonlinearity of the structure. To facilitate the convergence, a lift-up process of SCR is performed to achieve the SCR installation configuration before the global riser simulation as shown in Fig. 5. Initially, the SCR is modelled as a straight riser laying on the seabed with the anchor point fixed at the coordinates (0, 0) and the other end of the SCR located at Position A (2000, 0). The seabed is modelled as rigid to avoid any unrealistic soil disturbance. In the next step, the SCR is lifted from Position A to Position B, and the seabed remains rigid. Then similar steps are repeated to lift the top end of the SCR from B to E. After the top end of the SCR reaches the hanging-off point (HOP) (1460, 920), the rigid seabed model is removed, and the nonlinear seabed (i.e., the pipe-soil model) is activated. In this stage, the initial incursion of the riser into the seabed is established, and the configuration of the SCR, with a hang-off angle of 15.7°, is achieved during the installation.

3.2. Concept for fatigue analysis

The fatigue analysis method based on *S-N* curves has been widely used in structural design [30]. It is assumed that the fatigue damage of a material can be described by an *S-N* equation given as

$$N = A(\Delta\sigma)^{-m} \tag{12}$$

where N is the allowable number of cycles to failure for stress range $\Delta\sigma$, and m and A are material constants, which are determined from fatigue tests.

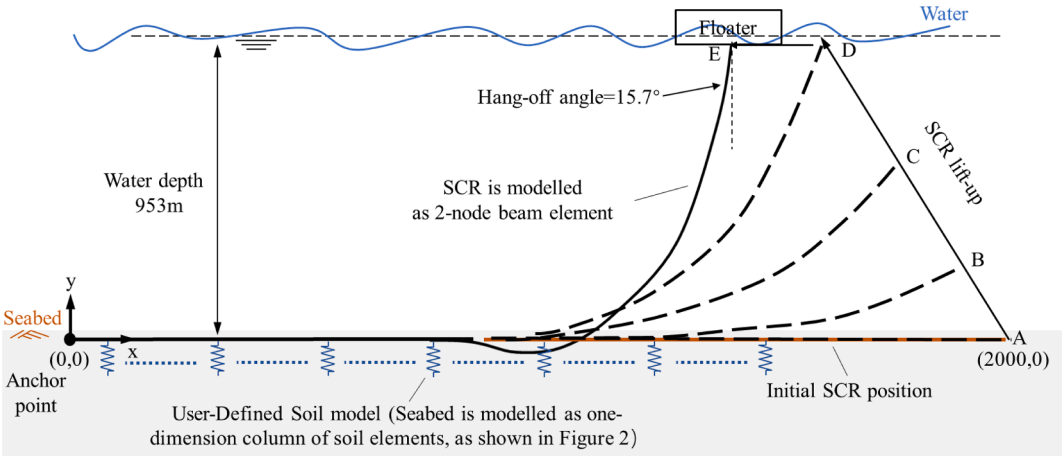

Fig. 5. Schematic demonstration of the global riser installation.

In the present analysis, the DNV *S-N* curve 'C' in seawater with cathodic protection [31] is used, which is a two-segment *S-N* curve as shown in Fig. 6. To calculate the stress range of the riser, the linear combination of the bending and axial stresses is used as fatigue stress according to DNV-RP-F204 [32].

$$\sigma_c = \sigma_a + \sigma_b \tag{13}$$

where σ_a is the axial stress due to the tension and σ_b is the bending stress.

With the *S-N* curve fatigue approach, the fatigue life can be calculated based on the Palmgren-Miner rule [33], which assumes that cumulative fatigue damage is a linear summation of the individual damage from all the considered stress range intervals, i.e.,

$$D_b = \sum_{i=1}^{b} \frac{n_i}{N_i} \tag{14}$$

where D_b is the accumulated fatigue damage; b is the number of stress blocks; n_i is the number of stress cycles in stress block i and N_i is the number of cycles to failure at constant stress range $\Delta\sigma_i$.

4. Case study

In this section, a case study employing the proposed global SCR model is provided to demonstrate its merit. Before the simulation, the validity of the pipe-soil model is first confirmed by comparing its outcomes with the SCR segment tests reported by Yuan et al. [34] and Zhou et al. [29], ensuring the accurate representation of pipe-soil interactions.

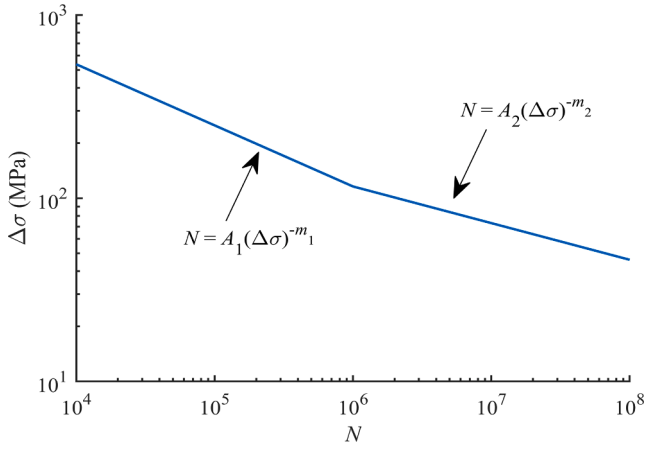

Fig. 6. S-N curve used in the study ($A_1 = 1.56 \times 1012$, $m_2 = 3$, $A_2 = 2.09 \times 1016$, $m_2 = 5$).

Following that, the precision and reliability of the global riser model, which incorporates the UEL for the pipe-soil model, are verified through a comparison with simulation data by industry-standard software, Flexcom. Lastly, the global response of the SCR, with its HOP subjected to 1000 harmonic motion cycles induced by spar heave motions, is examined. The primary focus is on the progressive embedment of the riser and the force–displacement response for various riser segments at the TDZ.

4.1. Model parameters and the simulation case

The parameters of the pipe-soil model are summarised in Table 3.

Table 3
Parameters of pipe-soil model.

Framework component	Parameter	Description	Value
Geometry	D	Diameter of SCR (prototype scale)	0.457 m
Soil characteristics	γ'	Effective unit weight	6 kN/m^3
	OCR	Over-consolidation ratio	1
	S_t	Sensitivity	4 (10, 20) *
Critical state mode	λ	Compression index	0.205
	κ	Swelling index	0.044
	Λ	Plastic volumetric strain ratio	0.6
	$(s_u/\sigma'_{vo})_{NC}$	Normally consolidated undrained strength ratio	0.16
	Γ_{NCL}	Specific volume, v, at σ'_v = 1 kPa on NCL	3.251
Excess pore pressure generation	ε_{99}	Cumulative shear strain parameter	600
	p	Shear strain rate parameter	2.95
	β	Strain influence zone extent	0.5D
Consolidation process	T_{50}	Non-dimensional time for 50% consolidation	0.09
	m	Embedment level parameter	1.4
General soil strength and stiffness response	Φ_{steady}	Strength parameter at steady, remoulded conditions	0.6 (1.2, 1.8) **
	α	Strength influence zone extent	0.5D
	K_{max}	Maximum tangent stiffness	200
	ς	Power law parameter for strength mobilisation	0.32

* Note. The sensitivity of 4 is used in the base case, while the values of 10 and 20 are used for investigating the influence of soil sensitivity.

** Note. The Strength parameter of 0.6 is used in the base case, while the values of 1.2 and 1.8 are used for investigating the influence of soil strength gradient.

The soil basic properties (γ', OCR) and the critical state parameters (λ, κ, Λ, Γ_{NCL}, and $(s_u/\sigma'_{vo})_{NC}$) are originated from the standard geotechnical lab/penetrometer tests [34–36]. Soil sensitivity $S_t = 4$, is determined from the cyclic penetration and extraction test by Yuan et al. [34] with a bearing capacity factor $N_{T\text{-}bar} = 10.5$ [37]. The characteristic strain $\varepsilon_{99} = 600$ and the control parameter $p = 2.95$ for depicting the excess pore pressure generation are used as suggested by Zhou et al. [10] to capture the additional reduction in seabed strength and stiffness induced by water entrainment.

For delimiting the shear strain influence zone and the strength influence zone, $\alpha = 0.5$ and $\beta = 0.5$ are adopted respectively based on the failure mechanism reported by Randolph and White [22]. The maximum tangent stiffness, $K_{max} = 200$ and power law parameter $\varsigma = 0.32$ are determined by giving a good agreement against the measured pipe-soil interaction in the pipe test [34].

In the global SCR simulation, only the heave motion of the spar is considered, thus causing the top end of the SCR to move vertically in the y-direction correspondingly. A regular heave motion with an amplitude of $H = 2.0$ m and a period of 10 s is applied at the HOP of the SCR. A time-domain dynamic simulation consisting of 1000 heave motion cycles is carried out. The areas surrounding the touch-down point (TDP) and touch-bottom point (TBP) have been identified as crucial for soil disturbance, as corroborated by previous studies [15,17].

The cases performed in the present study are listed in Table 4. Firstly, the pipe-soil model and the global riser model are validated through *Validation I* and *Validation II*, respectively. Based on the validated models, the penetration resistances of different SCR segments at the TDZ are examined with the global simulation (referred to as *Case for PSI*). Following this, the effects of three critical design parameters on the interaction between the pipe and soil with the inclusion of trench development, seabed strength and floater heave motion are investigated through the *Cases for global riser responses*. It's worth noting that in the case for the water entrainment effect, the high value of S_t is utilised (reported by Zhou et al. [29] and Yuan et al. [34]).

4.2. Validation of pipe-soil interaction model and global riser model

Before simulating the global SCR, the pipe-soil model to simulate the behaviour of a segment of the SCR under cyclic loading was validated against SCR segment tests reported by Yuan et al. [34] and Zhou et al. [29], which included both displacement-controlled and load-controlled tests. After implementing the effective stress framework in the UEL subroutine, a single user element was tested in Abaqus simulations by applying forced displacement to the user element for the displacement-controlled tests and applying concentrated force to the user element for the load-controlled tests. As this study primarily concentrates on soil remoulding, only the "short-term" test was considered.

In the displacement-controlled test, the pipe segment was penetrated from a normalised depth of $\widehat{z} = -1$ (one diameter above the mudline) to $\widehat{z} = 3$ for 200 loading cycles. The comparison between the simulated results and experimental measurements from Zhou et al. [29] is presented in Fig. 7. For this 'mudline-breaking' test, where each cycle crosses the water-mudline interface, the continuous water entrainment during the cyclic loading leads to a lower soil strength than the fully remoulded soil strength. In the effective-stress framework model, this phenomenon can be accurately captured by assigning a higher soil sensitivity, S_t, then shifting the fully remoulded strength line, RSL, to the 'lift side' in a specific volume-effective stress space (Fig. 3b), which represents cyclic 'mudline-breaking' induced lower effective stress and in turn a lower seabed strength (see Fig. 3e). With the simulated changing seabed strength by the effective-stress framework, the SCR penetration resistance q_s is calculated through Eqs. (7)–(10). The normalised $q_{s,N}/q_{s,1}$ (where N is cycle number) against cycle number at a normalised depth of $\widehat{z} = 2$ is presented in Fig. 7(a). The result indicates that the effect of water entrainment on the changing penetration resistance is well captured by the model in comparison to the measured data. The profiles of penetration and extraction SCR penetration resistance at different cycle numbers also demonstrate good agreement as illustrated in Fig. 7(b). In the load-controlled test, the pipe segment was penetrated from $\widehat{z} = -1$ to a depth where the penetration resistance q is equal to 8 kPa and then extracted for 100 cycles. As Fig. 7(c) shows, experimental observations of the progressive penetration depth at $q = 8$ kPa, indicating the degradation of the soil strength and stiffness due to the remoulding and water entrainment, are effectively mimicked by the proposed model. The penetration resistance profiles exhibit good agreement between the simulations and the measurements at $N = 1$, 2, 10, and 100 (noting that cycle 10 are unpublished data from the test reported by Yuan et al. [34], but presented by Zhou et al. [29]), which indicates that the pipe-soil interaction model is successfully implemented in the UEL subroutine.

The proposed global riser model is validated against results from an industry-standard design tool employed to simulate the installation response of a riser from the HOP to the seabed. It is worth mentioning that the existing design tools are not able to account for cycle-by-cycle induced seabed degradation. Therefore, only the installation phase is considered in the validation. The post-installed configuration of the SCR is depicted in Fig. 8 and compared with the global SCR profile obtained from Flexcom – a commercial riser dynamics solver utilising the same seabed properties. Both models show the same SCR profile and the deepest penetration of about 0.2 m along the TDZ. This comparison demonstrates that the proposed global riser model can accurately capture both the global response and the local curvature at the TDZ of the riser. In the next section, results from additional analyses considering cyclic loading will be discussed to further emphasise the model's merits.

Table 4
Simulation cases.

Analyses	k (kPa/m)	S_t	H (m)	Remarks
Validation I	1	4	–	Pipe-soil model simulation against Yuan et al. [34]
Validation II	1	4	–	Global riser model against Flexcom
Case for PSI	1	4	2	SCR penetration resistance
Cases for global riser responses	1 2 3	4	2	Effect of seabed strength and stiffness
	1	4 10 20	2	Effect of water entrainment
	1	4	1 2 3	Effect of heave motion

4.3. Results and discussion

For the global simulation *Case for PSI*, the SCR profiles at different cycle numbers (N) are illustrated in Fig. 9. Following the installation, the SCR comes into contact with the seabed at the TBP of −0.24 m (note that the negative value represents soil depth). As cyclic loading occurs, the embedded riser progressively penetrates, reaching a relatively stable position at $N = 1000$. The SCR profiles at the TDZ are presented as a "ladle" shape, and the TBP moves 0.37 m towards the anchor point and the TDP moves 3.5 m towards the HOP. This process can be attributed to the generation of excess pore pressure induced by cyclic loading, which consequently decreases the effective stress and seabed strength, and the expanding influence zone at the TDZ serves to redistribute the load along the SCR.

The force–displacement responses of four nodes (node 903, node 928, node 953 and node 981) at different riser sections in the TDZ are presented in Fig. 10. Note that in the subfigures, the y-axis represents the penetration depth, and the x-axis represents the penetration resistance.

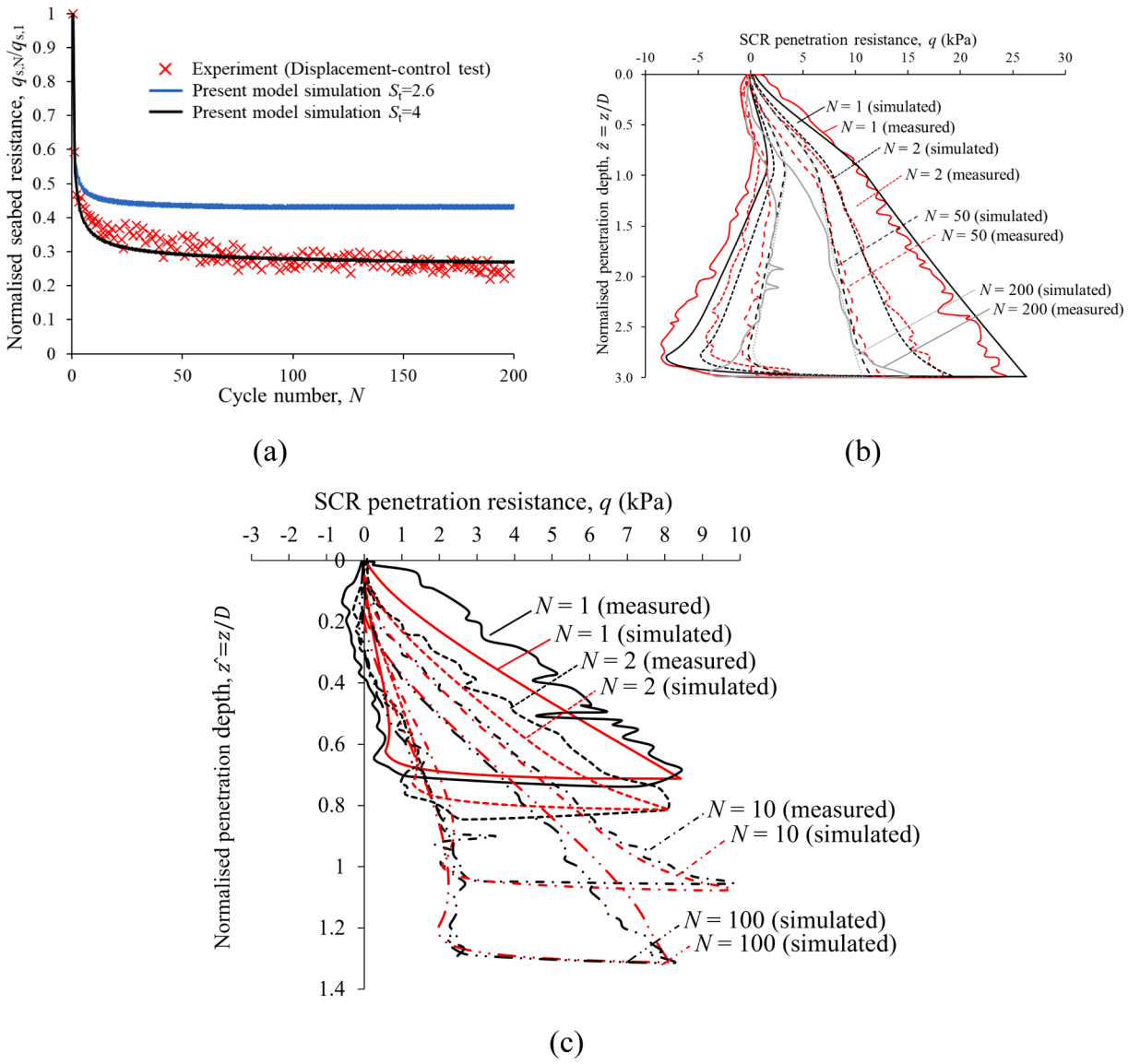

Fig. 7. Validation for pipe-soil model against experimental observation conducted by Zhou [29]: (a) normalised seabed resistance against number of cycles; (b) SCR penetration resistance profiles against depth for displacement-controlled tests; (c) SCR penetration resistance profiles against depth for load-controlled tests.

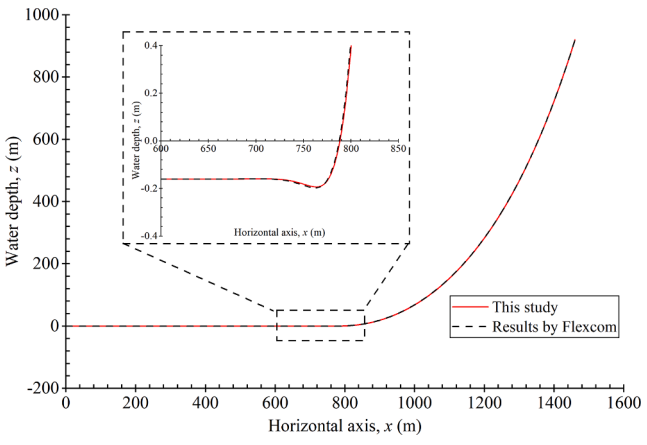

Fig. 8. Verification for the global riser model against Flexcom.

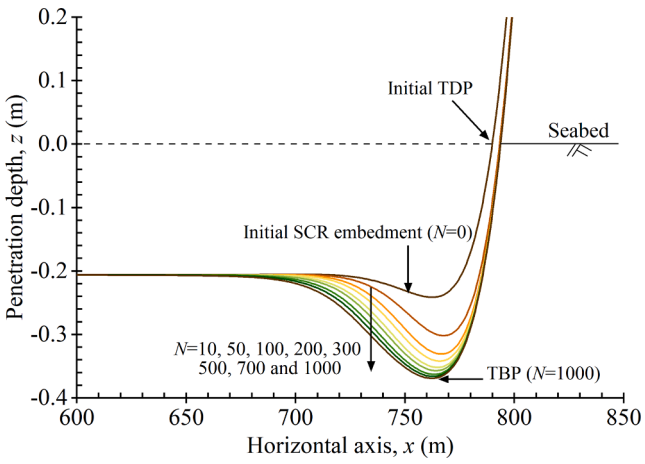

Fig. 9. Global riser profiles at different cycle numbers.

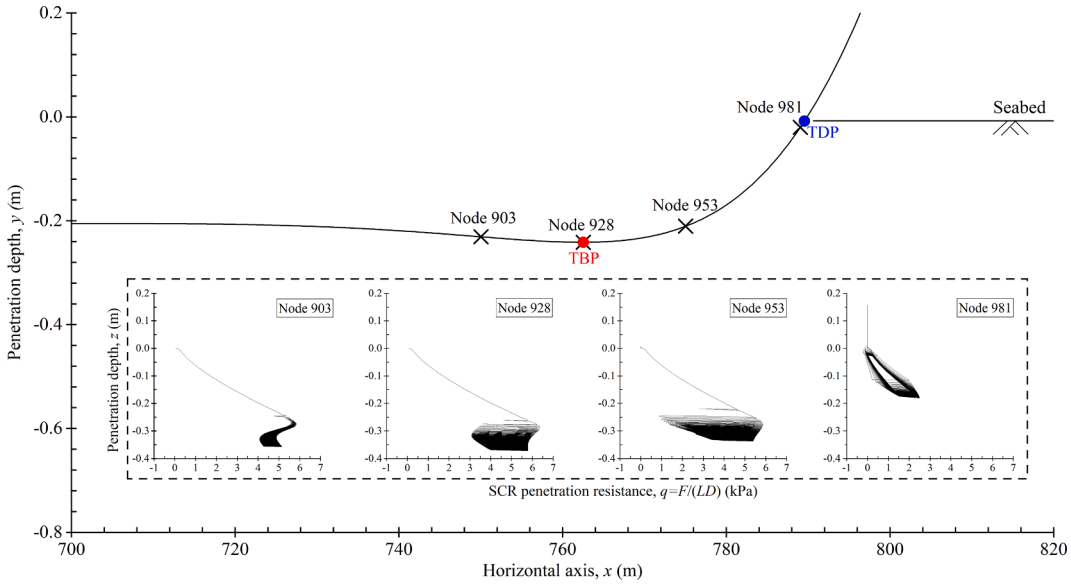

Fig. 10. Force – displacement responses along the riser (The penetration reaction force F on a beam element is normalised by the riser diameter D and the element length L).

The force–displacement curves of the four nodes display distinct shapes, reflecting the diverse behaviour of the pipe elements at the TDZ in response to the soil remoulding process caused by varying amplitudes of pipe displacement. From a global perspective, higher penetration resistance is mobilised for riser segments with deeper penetration depths, such as node 903, node 928, and node 953, while just under 3 kPa is mobilised for node 981.

Node 981, which is considered as the TDP and located around the mudline, experiences significant cyclic motions at a shallow depth. During each cycle, the pipe segment must penetrate deeper to mobilise a higher soil strength, resulting in a series of hysteresis loops. As the number of cycles increases, the hysteresis loops become “slimmer”, indicating deeper penetration and smaller variations in the penetration resistance when the soil strength is fully remoulded. In contrast, Node 953, which is located at a deeper site with a much smaller motion amplitude than Node 981, exhibits a force–displacement curve with a different shape, where hysteresis loops have not formed. This can be attributed to the deep installation embedment of the SCR segment, where the seabed strength is high and load equilibrium is achieved, even though the geotechnical resistance is not fully mobilised. A similar force–displacement curve is observed for Node 928, which is located at the lowest depth, and the variation in penetration resistance during each cycle is smaller than that of Node 953 due to the lowest cyclic displacement. In both cases, the pipe segments gradually penetrate deeper under cyclic loading, representing a cyclic degradation of soil strength, and ‘fresh’ soil is also mobilised with higher shear strength. For Node 903, which is located on the edge of the cyclic influence zone, the motion amplitude and penetration resistance are initially very small since most of the cyclic loading is resisted by the soil along the embedded SCR. However, as the load is redistributed and the cyclic influence zone expands, the penetration force at Node 903 increases, accelerating the soil remoulding process in the later cycles.

5. Key design factors for riser fatigue analysis

This section focuses on assessing the effects of design parameters on the global riser-seabed interaction and the degradation of seabed resistance. Additionally, the dynamic responses of the global riser, such as shear force and bending moment at the TDZ, are evaluated. The stress time history for the most critical node is also presented, and fatigue damage is calculated using the S-N curve. The primary objective of this analysis is to gain insight into the influence of these design parameters on pipe-soil interaction and the overall structural response of the system. This will ultimately assist in identifying critical design parameters and refining the design process for SCRs.

5.1. Effect of trench development

Fig. 11 presents the SCR profiles following 1, 10, and 1000 heave motion cycles, alongside contours of soil effective stress with different values of S_t. The initial soil strength, $s_{u,i}$, is consistent for all three simulations, but varies with S_t, resulting in soil strength degradation even lower than remoulded soil strength. The cyclic loading applied to the riser allows seabed softening towards a steady state with continuous penetration of the pipeline. Fig. 11(b) demonstrates that a higher soil sensitivity (i.e., $S_t = 20$) leads to a higher reduction in effective stress, thereby a lower soil strength under the cyclic loading. The soil in the vicinity of the TBP is fully remoulded after 1000 cycles, during which the effective stress is reduced by approximately 15 times for $S_t = 4$ (and 75 times for $S_t = 20$), and values of $\sigma'_{v,RSL}$ for both $S_t = 4$ and $S_t = 20$ are much lower than $\sigma'_{v,NCL}$. Additionally, it is important to note that the cyclic influence zone expands with the limited range from a depth of −0.32 m at $N = 1$ to −0.57 m at $N = 1000$. This implies that the redistribution of the cyclic force along the SCR cannot generate free expansion of the pipeline along the horizontal direction at the TDZ, though the soil is softened. Therefore, under the same heave motion of the floater, only a slight difference in the riser profile is detected, with a slightly deeper TBP achieved for higher S_t.

Fig. 12 displays the mean shear forces and bending moments at the TDZ following 1000 motion cycles. The SCR profiles with varying S_t exhibit slightly different curvatures within the range of 700 m to 750 m of the SCR arc length as a result of the penetration force redistribution along the SCR, leading to corresponding variations in mean shear forces and bending moments within this range. However, the distributions of mean shear force and bending moments at other length ranges remain essentially identical.

To investigate the impact of the soil sensitivity on the fatigue damage of the SCR, the distribution of the fatigue damage in the TDZ is demonstrated in Fig. 13 (b). Notably, the fatigue damage curve exhibit two distinct peaks. The first peak corresponds to the TDP, arising from the interaction between the seabed and SCR. The second peak is observed approximately 30 m away from the TDP, towards to the hang-

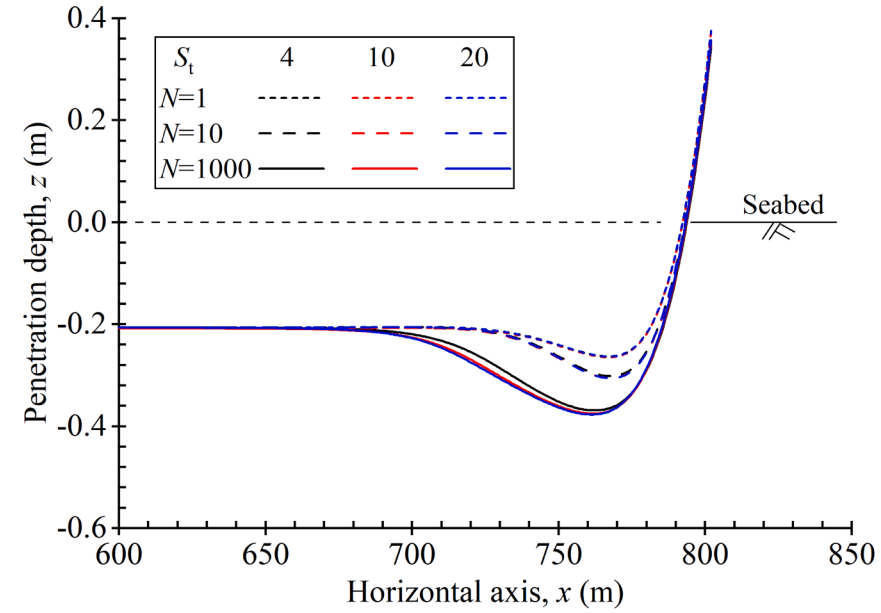

(a)

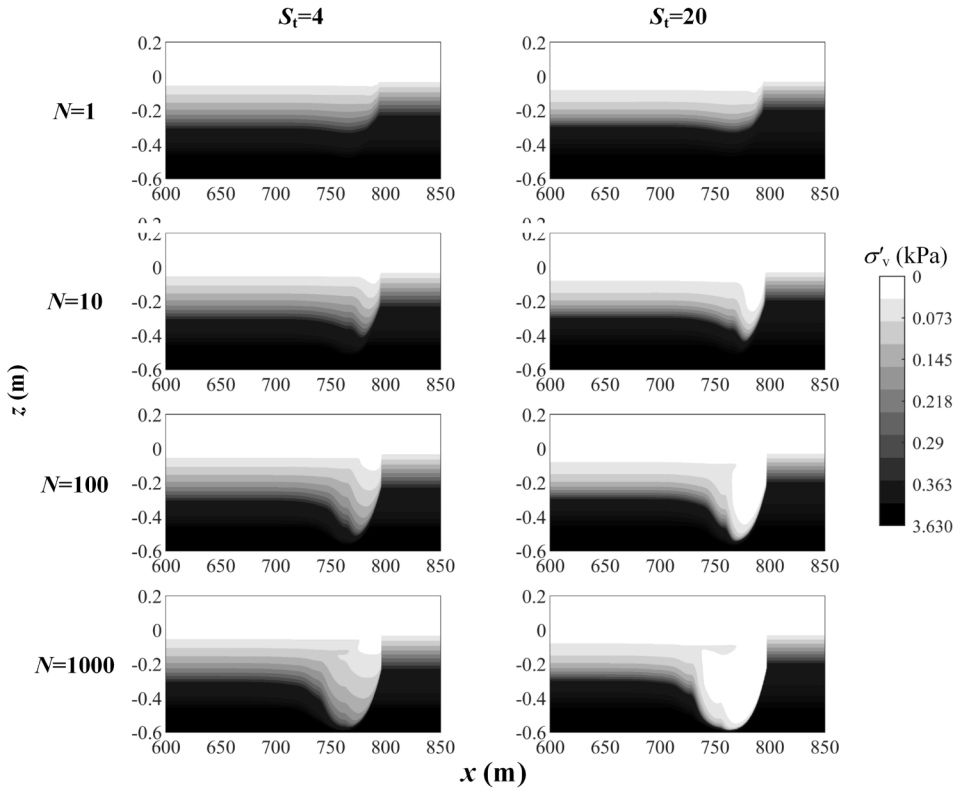

(b)

Fig. 11. Penetration and trench development with different soil sensitivity values ($k = 1$ kPa, $H = 2$ m): (a) Progressive penetration of SCR; (b) Effective stress of soil.

off point. This second peak is attributed to the significant sag bend, serving as a transition from the seabed supporting point (i.e., TDP) to the nearly vertical suspension. During platform heave motion, the vibration of this transition segment is primarily dominated by the radial motion of the SCR, resulting in a large dynamic bending stress range and consequently higher fatigue damage. On the other hand, in the nearly vertical suspension region, the SCR motion is primarily axial under the forced platform heave, leading to significantly lower fatigue damage. This distinct pattern of two peaks in fatigue damage aligns with findings from dynamic simulations conducted by Yuan et al. [38].

In the present study, the most critical spot of the SCR is identified as the TDP, and the stress time history of this hot spot is shown in Fig. 13(a) for cycles 995 to 1000. It can be observed that the stress range at this hot spot decreases slightly as the soil sensitivity increases, leading to a

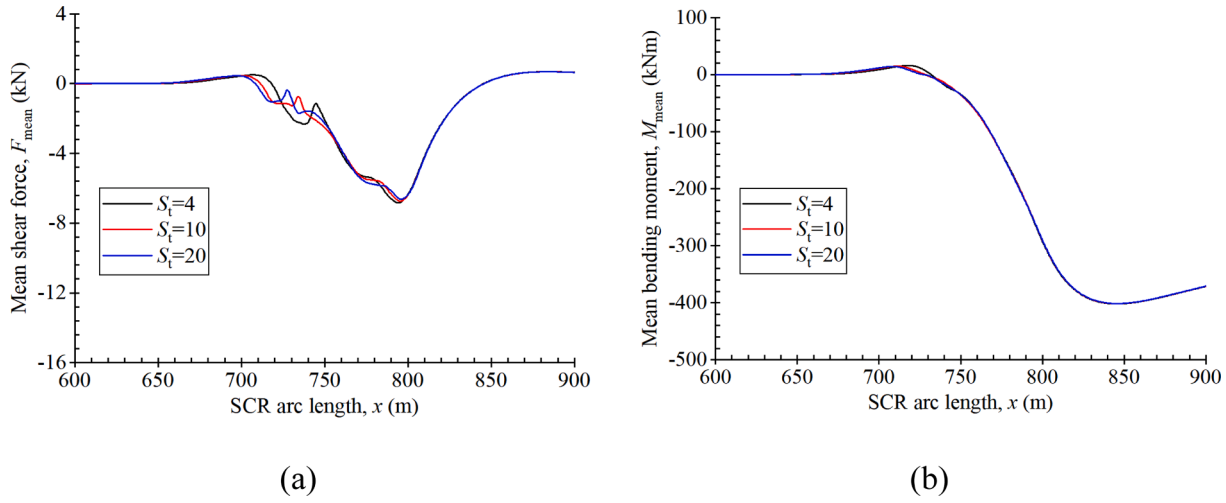

Fig. 12. Responses of the global riser with different soil sensitivity values (k = 1 kPa, H = 2 m): (a) Mean shear force; (b) Mean bending moment.

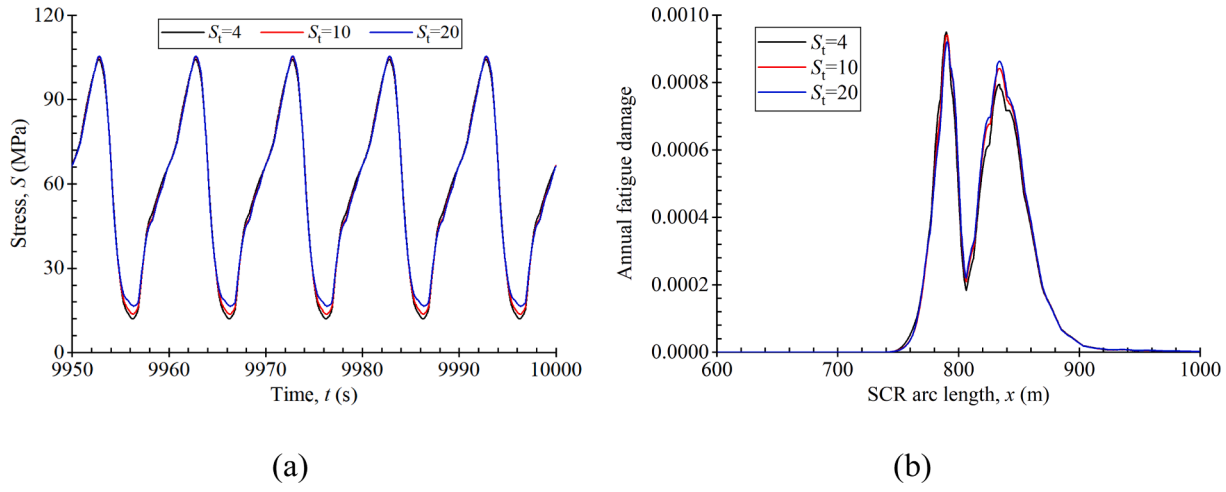

Fig. 13. Responses of the hot spot with different soil sensitivity values (k = 1 kPa, H = 2 m): (a) Stress; (b) Fatigue damage.

corresponding decrease in fatigue damage correspondingly as shown in Fig. 13(b). This indicates that the influence of water entrainment on the SCR responses is limited to this hot spot because of the significant redistribution of the cyclic load along the SCR. Moreover, the softened seabed strength induced by the large water entrainment is actually beneficial to the fatigue life of the TDP. However, an increase of the fatigue damage is observed at the second peak of the fatigue damage curve with the increasing soil sensitivity.

5.2. *Effect of seabed strength*

Fig. 14 shows the simulated SCR profiles and contours of the soil effective stress after 1, 10 and 1000 heave motion cycles. Three different seabed strength gradients, k (defined as ds_u/dz) of 1, 2 and 3 kPa/m, representing soft, intermediate, and hard seabed conditions. In the study, to simulate elevated soil strength gradients of k = 2 and 3 kPa/m, increased values of the strength parameter Φ_{steady} were employed (Φ_{steady} = 1.2 for k = 2 kPa/m; Φ_{steady} = 1.8 for k = 3 kPa/m). This approach enabled an elevation in soil strength at the same effective stress level.

As expected, a higher seabed strength will result in greater penetration resistance, leading to shallower riser embedment during the first cycle. As the sensitivity of soil S_t is consistent across all three cases, the soil strength will degrade to different levels, with the remoulded soil strength for the soft seabed being lower than that for the hard seabed. As a result, a deeper riser embedment is also observed for the soft seabed (i.e., k = 1 kPa/m) after multiple cycles.

During the dynamic loading phase, the SCR gradually penetrates into the seabed as the soil strength is cyclically remoulded, eventually reaching a stable depth where the remoulded strength can resist the SCR loading, as shown in Fig. 14(a). However, due to the movement of the riser and the redistribution of loading during progressive riser penetration at the seabed, some pipe segments cannot carry the same load amplitude indefinitely. The interaction between the SCR and the seabed will cause the flexible riser to redistribute the intensity of load acting on the seabed. For a hard seabed condition in this study (i.e., k = 3 kPa/m), the load concentrated in the vicinity of the TBP is difficult to release towards the anchor point during cycles (i.e., movement in the horizontal), and the SCR is confined in a narrow trench, resulting in a significant increase in the embedment depth at the bottom of the SCR, as shown in Fig. 14(b). As a result, a deeper soil remoulding region is observed for the seabed with k = 3 kPa/m between 760 m and 800 m.

Fig. 15 compares the mean shear forces and bending moments with different seabed strengths at the TDZ after 1000 cycles. Due to the different configurations and penetrations of the SCR under different seabed conditions, a noticeable change in the mean shear forces and bending moments is observed in the range of riser length from 700 m to 750 m. As the seabed strength increases, the variation of the mean force

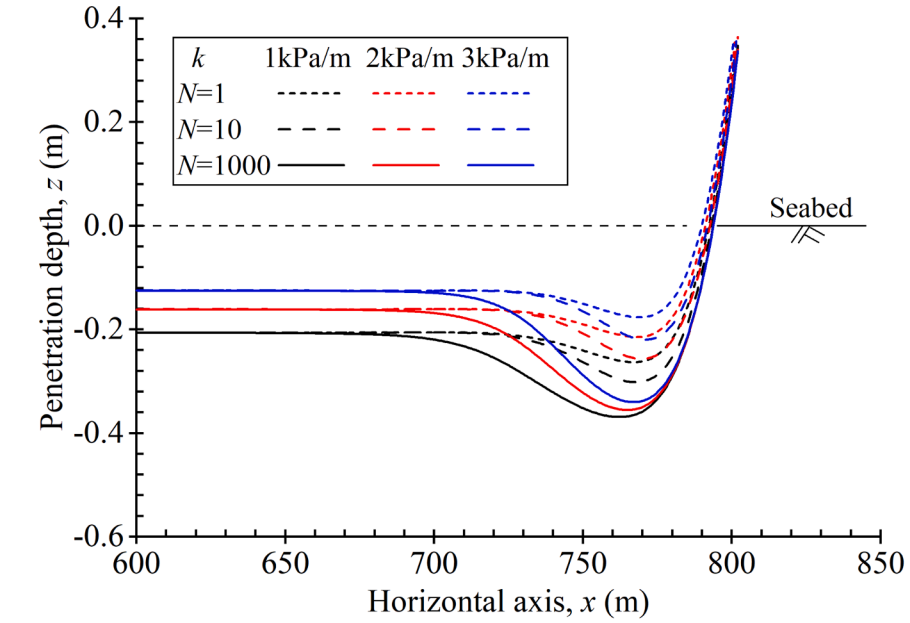

(a)

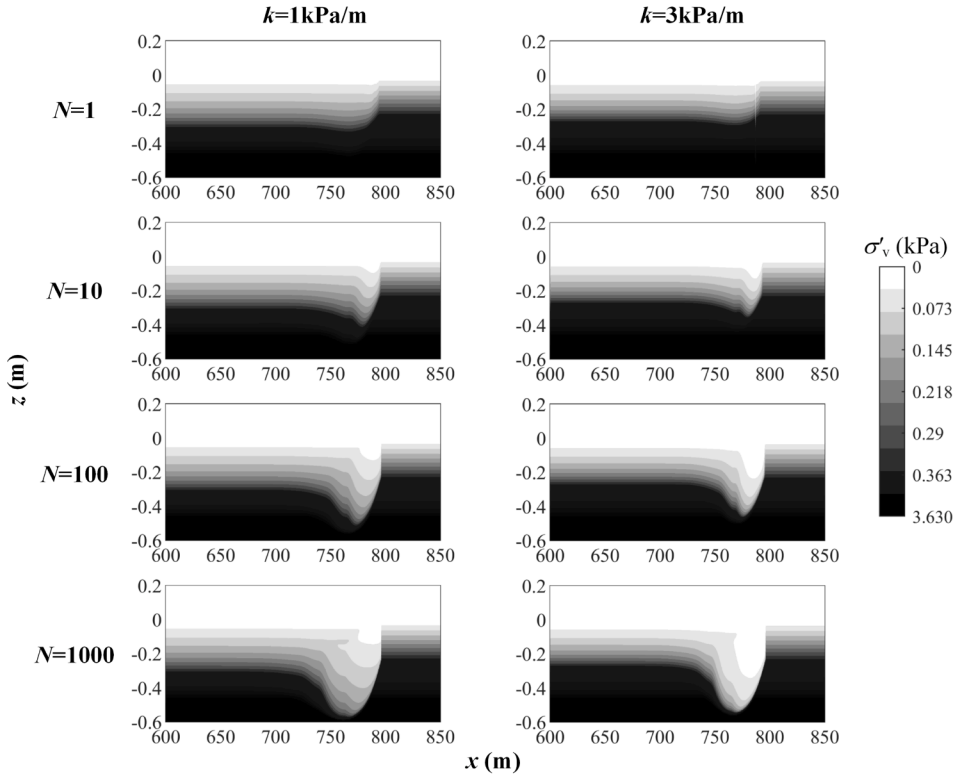

(b)

Fig. 14. Penetration and trench development with different seabed strengths (S_t = 4, H = 2 m): (a) Progressive penetration of SCR; (b) Effective stress of soil.

becomes larger and the force peak shifts towards the TDP, with a similar trend observed for the peak of the mean bending moment. This can be attributed to the fact that a softer soil results in a smaller change in curvature at the riser length range from 700 m to 750 m, while a stiffer soil tends to confine the riser to a narrower trench, resulting in a larger change in curvature. This conclusion is similar to that drawn by Dong and Shiri [17].

The stress time histories of the hot spot for the three cases (located at x = 789 m), are compared in Fig. 16(a). It can be observed that both the stress troughs and crests increase with the seabed strength and stiffness though the increase is not very significant. Correspondingly, the first fatigue damage peak increases with the seabed stiffness as shown in Fig. 16 (b), and the second fatigue damage peak demonstrates a similar trend. These results indicate that a stiffer seabed leads to a larger

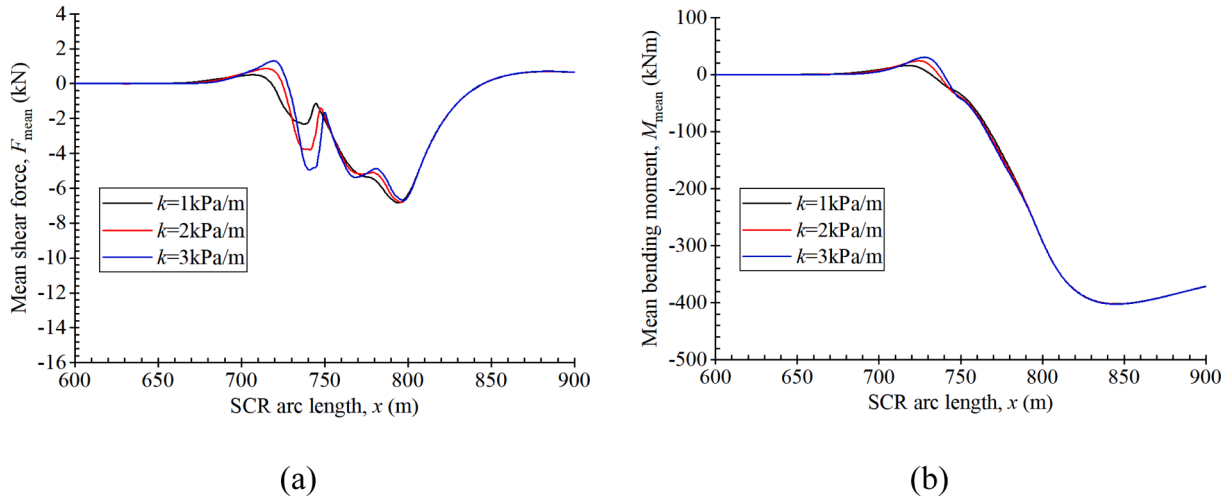

Fig. 15. Responses of the global riser with different seabed strengths ($S_t = 4$, $H = 2$ m): (a) Mean shear force; (b) Mean bending moment.

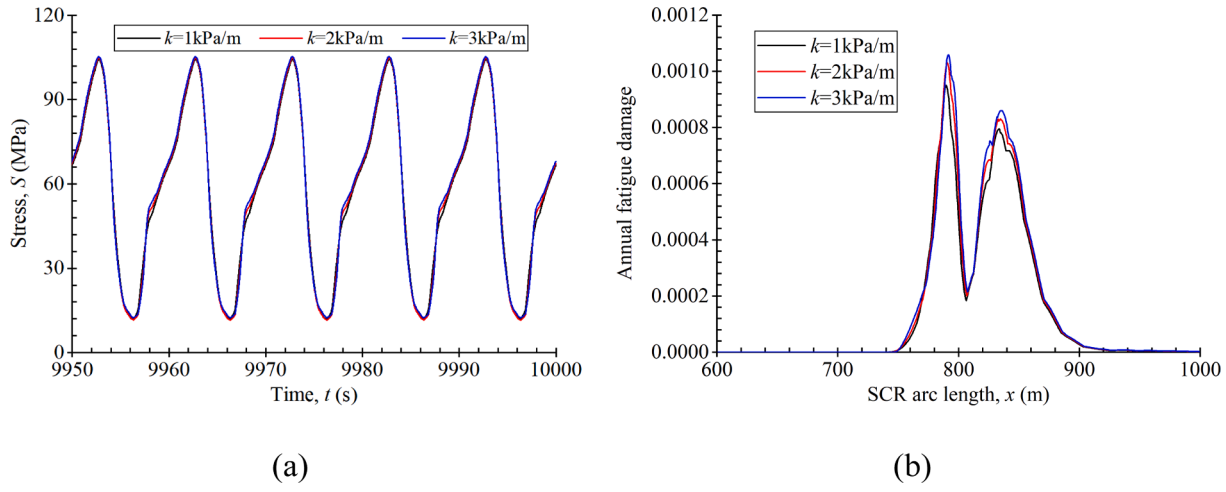

Fig. 16. Responses of the hot spot with different seabed strengths ($S_t = 4$, $H = 2$ m): (a) Stress; (b) Fatigue damage.

curvature and higher fatigue damage at the hot spot, which is consistent with the conclusion reached by Bai et al. [15].

5.3. *Effect of heave motion*

The effect of the floater heave motion is investigated by varying the heave amplitude H from 1 m, 2 m to 3 m. Fig. 17 presents the SCR profiles and contours of soil effective stress for different heave amplitudes after 1, 10 and 1000 heave motion cycles. The heave motion amplitude of the floater has a significant influence on the riser profile. As the heave motion amplitude increases, the position of the TDP is shifted to the right side, while the TBP location is shifted to the left, and a deeper trench development is observed. As the cycle number increases, the remoulded region of the effective stress expands more extensively. However, as S_t is kept consistent and the seabed is relatively soft ($k = 1$ kPa in this case), the force concentrated on the TBP is more easily transmitted towards the anchor point, resulting in less degradation of the effective stress of the soil along the downwards direction.

The mean shear forces and bending moments with different heave motion amplitudes after 1000 cycles are shown in Fig. 18, which demonstrates distinct peak values and corresponding locations along the embedded riser in the length range from 700 m to 750 m. In contrast to the effect of seabed strength, the variation in the mean shear force decreases and the force peak shifts towards the anchor point with the increasing heave motion amplitude. This can be attributed to the greater penetration of the SCR in the length range of 700–750 m as the heave motion amplitude increases, resulting in a more pronounced curvature change in the riser at this section.

The stress time history curves of the hot spot subjected to different heave motion amplitudes are compared in Fig. 19. As expected, the large motion amplitude causes violent fluctuations in the stress. Consequently, the stress range and the corresponding fatigue damage increase significantly with the heave motion amplitude. Notably, the increase of the heave motion amplitude can relocate the most critical spot of the SCR from the TDP to the suspension point away from the TDP as shown in Fig. 19(b).

6. Conclusions

This study presents the development of a global SCR model incorporating an effective-stress framework for accurate analysis of pipe-soil interaction. The established model provides a basis for predicting the evolving seabed strength and dynamic structural response of SCR at the TDZ. By conducting a series of time-domain dynamic simulations on the global riser model, the study focuses on investigating the effects of three critical design parameters. The following key conclusions are drawn from the analysis:

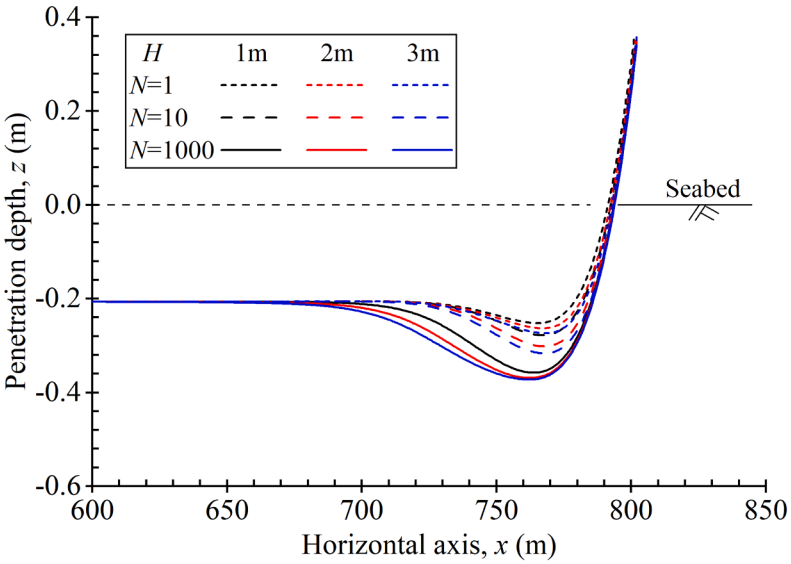

(a)

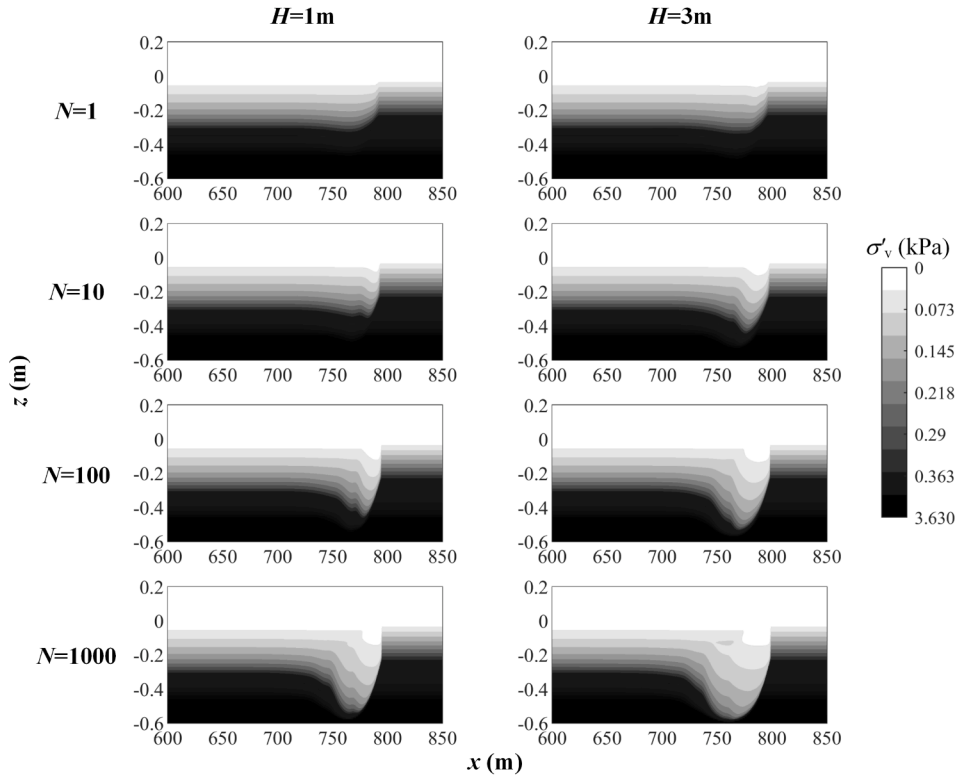

(b)

Fig. 17. Penetration and trench development with different heave motion amplitudes ($S_t = 4$, $k = 1$ kPa): (a) Progressive penetration of SCR; (b) Effective stress of soil.

1. The simulations capture the soil remoulding process and show that the global riser profiles change gradually with the penetration process. A stable penetration profile can be achieved after a sufficient number of SCR motion cycles, but different pipe segments at the TDZ exhibit different force–displacement responses. The segments near the TDP experience frequent interaction with the mudline, resulting in hysteresis loops in the force–displacement curves. Deeper segments, however, exhibit smaller response amplitudes with no hysteresis loops formed. Over cycles, the influence zone expands, and the segments far from the TDP become mobilised, redistributing the load along the SCR;
2. The riser profile is not highly sensitive to water-entrainment-induced seabed trench, and the stress of the TDP tends to decrease with increasing trench depth due to a significant redistribution of the dynamic loading along the SCR, but an increase of the stress at the transition (from TDP to suspension) segment is observed;
3. Higher seabed strength results in greater penetration resistance, which leads to a relatively shallow embedment of the SCR. At the

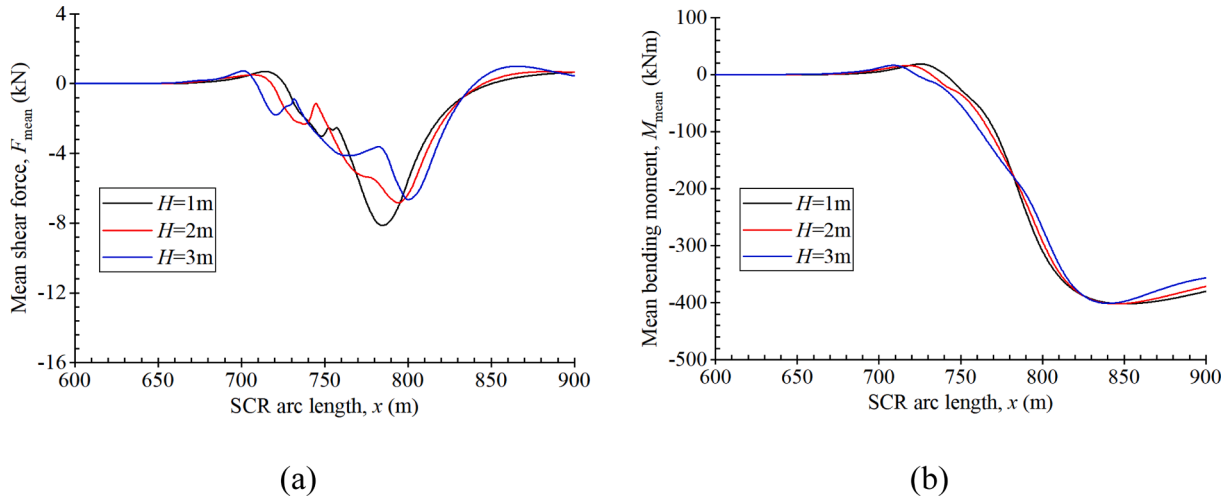

Fig. 18. Responses of the global riser with different heave motion amplitudes ($S_t = 4$, $k = 1$ kPa): (a) Mean shear force; (b) Mean bending moment.

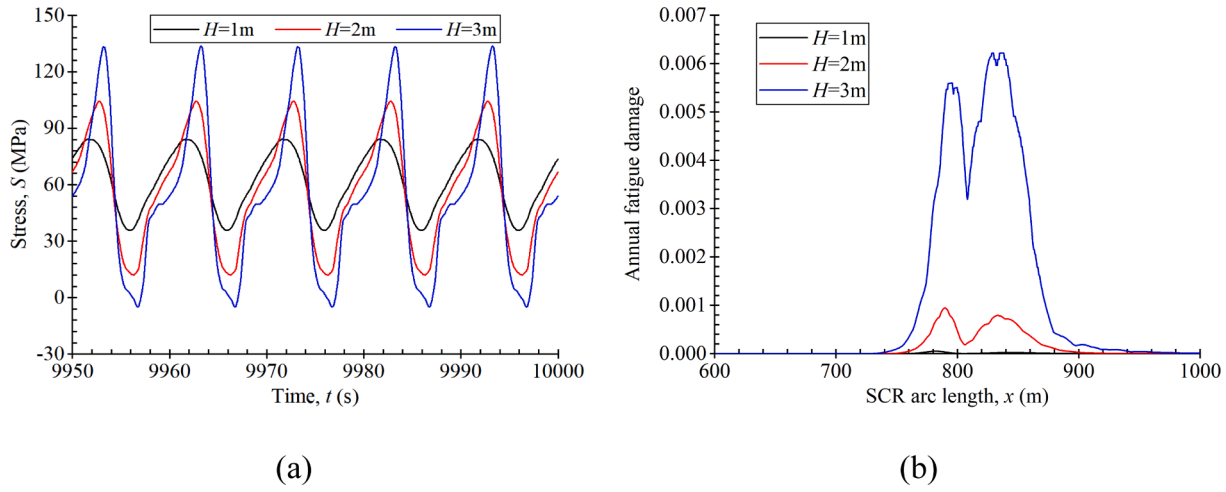

Fig. 19. Responses of the hot spot with different heave motion amplitudes ($S_t = 4$, $k = 1$ kPa): (a) Stress; (b) Fatigue damage.

TDZ, the remoulded region at the TDZ becomes narrower and deeper with increasing seabed strength, as the load on the riser is less able to expand towards the anchor point. This causes a large curvature and in turn high fatigue damage for the riser;

4. Large floater heave motions result in significant vibrations of the riser, leading to high fatigue damage. Moreover, the development zone of the trench tends to expand towards the anchor point with increasing floater heave motions. These findings emphasise the importance of considering floater heave motions in the design and operation of SCR systems.

Overall, the insights provided by this study shed light on the dynamic behavior and fatigue damage of global SCR systems. The findings can inform future designs and operations of such systems, enhancing their efficiency and reliability.

CRediT authorship contribution statement

Zhenguo Gao: Conceptualization, Methodology, Software, Validation, Formal analysis, Writing – review & editing. **Weichen Wang:** Writing – original draft, Data curation, Visualization. **Zefeng Zhou:** Methodology, Software, Supervision, Conceptualization, Writing - review & editing. **Yue Yan:** Resources, Validation, Writing - review & editing. **Dhruba L. Pradhan:** Conceptualization, Methodology, Writing - review & editing.

Declaration of Competing Interest

The authors declare that they have no known competing financial interests or personal relationships that could have appeared to influence the work reported in this paper.

Data availability

Data will be made available on request.

Acknowledgements

The fourth author acknowledges the support of the National Natural Science Foundation of China (No. 52271290). The corresponding author would like to acknowledge his research funding provided by the Norwegian Geotechnical Institute and the Norwegian Research Council. The last author acknowledges the support from the DNV.

References

[1] Li FZ, Low YM. Fatigue reliability analysis of a steel catenary riser at the touchdown point incorporating soil model uncertainties. Appl Ocean Res 2012;38:100–10.

[2] Queau LM, Kimiaei M, Randolph MF. Dimensionless groups governing response of steel catenary risers. Ocean Eng 2013;74:247–59.
[3] Bridge C, Laver K, Clukey E, Evans T. Steel catenary riser touchdown point vertical interaction models. In: Proceedings of the offshore technology conference, Houston, TX, USA, paper no. 2004 OTC 16628.
[4] You J, Biscontin G, and Aubeny CP. Seafloor interaction with steel catenary risers. In: Proceedings of the 8th international offshore and polar engineering conference, Vancouver, British Columbia, Canada, 2008. no. ISOPE-I-08-303.
[5] Clukey EC, Zakeri A. Recent advances in nonlinear soil models for fatigue evaluation of steel catenary risers SCRs. In: Proceedings of the offshore technology conference, Houston, TX, USA, paper no. 2017 OTC 27627.
[6] Aubeny CP, Biscontin G. Seafloor-riser interaction model. Int J Geomech 2009;9 (3):133–41.
[7] Voie PE, Skeie G, Berganhaavik J. Importance rating of riser-soil interaction effects. In: Proceedings of the ASME 2014 33rd international conference on ocean, offshore and arctic engineering. 2014.
[8] Randolph MF, Quiggin P. Non-linear hysteretic seabed modelfor catenary pipeline contact. In: ASME 2009 28th international conference on ocean, offshore and arctic engineering. American Society of Mechanical Engineers Digital Collection, 2009.
[9] Zargar E A new hysteretic seabed model for riser-soil interaction. PhD thesis, The University of Western Australia, Perth, Australia, 2017.
[10] Zhou Z, White DJ, O'Loughlin CD. An effective stress framework for estimating penetration resistance accounting for changes in soil strength from maintained load, remoulding and reconsolidation. Geotechnique 2019;69(1):57–71. https://doi.org/10.1680/jgeot.17.p.217.
[11] Hodder MS, White DJ, Cassidy MJ. An effective stress framework for the variation in penetration resistance due to episodes of remoulding and reconsolidation. Geotechnique 2013;63(1):30–43.
[12] White DJ, Hodder M. A simple model for the effect on soil strength of episodes of remoulding and reconsolidation. Can Geotech J 2010;47(7):821–6.
[13] Shiri H, Randolph MF. The influence of seabed response on fatigue performance of steel catenary risers in touchdown zone. Am Soc Mech Eng 2010:63–72.
[14] Elosta H, Shan H, Incecik A. Trenching effects on structural safety assessment of integrated riser/semisubmersible in cohesive soil. Eng Struct 2014;77:57–64.
[15] Bai X, Huang W, Vaz MA, Yang C, Duan M. Riser-soil interaction model effects on the dynamic behavior of a steel catenary riser. Mar Struct 2015;41:53–76.
[16] Liu J, Kimiaei M, Randolph MBT-AIC on O. A new user defined element for nonlinear riser-soil interaction analysis of steel catenary riser systems. In: ASME international conference on ocean. 2016.
[17] Dong X, Shiri H. Performance of non-linear seabed interaction models for steel catenary risers, part II: global response. Appl Ocean Res 2019;82:158–74.
[18] Zhao L, Zhou Z, Wang D, Chen L. Numerical modeling approach for steel catenary riser behavior at touchdown zone. J Geotech Geoenviron Eng 2021:147 (6).
[19] Janbazi H, Shiri H. Investigation of trench effect on fatigue response of steel catenary risers using an effective stress analysis. Comput Geotech 2023;160: 105506.
[20] Wood DM. Soil behaviour and critical state soil mechanics. Soil Behav Crit State Soil Mech 1991.
[21] Merifield RS, White DJ, Randolph MF. Effect of surface heave on response of partially embedded pipelines on clay. J Geotech Geoenvironmental Eng 2009;135 (6):819–29.
[22] Randolph MF, White DJ. Pipeline embedment in deep water: processes and quantitative assessment. In: Proc. Offshore Technology Conf., Houston, Paper OTC 19128. 2008.
[23] Systèmes D. Abaqus analysis users' manual. Providence (RI): Simulia Corporation; 2010.
[24] Har SG. Modelling and analysis of riser-seabed interaction. Master thesis. Singapore: National University of Singapore; 2007.
[25] Shiri H. Response of steel catenary risers on hysteretic non-linear seabed. Appl Ocean Res 2014;44:20–8.
[26] Akula V, Datye D. Implementation of a nonlinear riser-soil interaction model for Abaqus, 2015, OMAE 2015-41201.
[27] Morison JR, Johnson JW, Schaaf SA. The force exerted by surface waves on piles. Petroleum Trans J Pet Technol 1950;2(05):149–54.
[28] DNV. DNV-RP-C205 Environmental conditions and environmental loads. 2019.
[29] Zhou Z, O'Loughlin CD, White DJ. An effective stress analysis for predicting the evolution of SCR-seabed stiffness accounting for consolidation. Geotechnique 2020;70(5):448–67. https://doi.org/10.1680/jgeot.18.p.313.
[30] Lotsberg I. Fatigue design of marine structures. 2016.
[31] DNV. DNV-RP-C203 Fatigue design of offshore steel structures. 2016.
[32] DNV. DNV-RP-F204 Riser fatigue. 2010.
[33] Miner M. Cumulative damage in fatigue. J Appl Mech 1945;67:A159–64.
[34] Yuan F, White DJ, O'Loughlin CD. The evolution of seabed stiffness during cyclic movement in a riser touchdown zone on soft clay. Geotechnique 2017;67(2): 127–37.
[35] Stewart DP. Lateral loading of piled bridge abutments due to embankment construction. PhD thesis. Perth (Australia): The University of Western Australia; 1992.
[36] Zhou Z, O'Loughlin CD, White DJ, Stanier SA. Improvements in plate anchor capacity due to cyclic and maintained loads combined with consolidation. Geotechnique 2020;70(8):732–49. https://doi.org/10.1680/jgeot.19.TI.028.
[37] Martin CM, Randolph MF. Upper-bound analysis of lateral pile capacity in cohesive soil. Geotechnique 2006;56(2):141–5.
[38] Yuan Y, Zheng M, Xue H, Duan Z, Tang W. Fatigue analysis of a steel catenary riser at touchdown zone with seabed resistance and hydrodynamic forces. Ocean Eng 2022;244:110446.
[39] Rui S, Zhou Z, Jostad HP, Wang L, Guo Z. Numerical prediction of potential 3-dimensional seabed trench profiles considering complex motions of mooring line. Applied Ocean Research 2023;139:103704. https://doi.org/10.1016/j.apor.2023.103704.